Research Square

Preprints are preliminary reports that have not undergone peer review.
They should not be considered conclusive, used to inform clinical practice,
or referenced by the media as validated information.

T4 Bacteriophage-Inspired Six-Legged Optical Fiber Sensor for Sensitive and Robust Micro-Airflow Detection

□□□□ □□□

msm-liu@126.com

Northeast Petroleum University https://orcid.org/0000-0001-6382-008X

Weiqiang Wang
Northeast Petroleum University

Jingwei Lv
Northeast Petroleum University

Famei Wang
Shenzhen Technology University

Xili Lu
Harbin Engineering University

Jianxin Wang
Northeast Petroleum University

Wei Liu
Northeast Petroleum University

Zao Yi
Southwest University of Science and Technology

Jianshe Li
Yanshan University https://orcid.org/0000-0002-9580-281X

Xinping Song
Northeast Petroleum University

Paul K. Chu
City University of Hong Kong https://orcid.org/0000-0002-5581-4883

Article

Keywords: T4 bacteriophage, biomimetic structure, fiber-optic sensor, Fabry–Pérot interference, micro-airflow detection, two-photon polymerization

Posted Date: November 20th, 2026

DOI: https://doi.org/10.21203/rs.3.rs-11598580/v1

License: This work is licensed under a Creative Commons Attribution 4.0 International License.
Read Full License

Additional Declarations: There is no conflict of interest

T4 Bacteriophage-Inspired Six-Legged Optical Fiber Sensor for Sensitive and Robust Micro-Airflow Detection

Chao Liu [1], Weiqiang Wang[1], Jingwei Lv[1*], Famei Wang[2], Xili Lu[3], Jianxin Wang[1], Wei Liu[1], Zao Yi[4], Jianshe Li[5], Xinping Song[1], Paul K. Chu[6]

[1] *School of Physics and Electronic Engineering, Northeast Petroleum University, Daqing 163318, China*

[2] *Shenzhen Key Laboratory of Ultra-Intense Laser and Advanced Material Technology, Center for Intense Laser Application Technology, and College of Engineering Physics, Shenzhen Technology University, Shenzhen 518118, China*

[3] *School of Materials Science and Chemical Engineering, Harbin Engineering University, Harbin 150001, China*

[4] *Joint Laboratory for Extreme Conditions Matter Properties, Southwest University of Science and Technology, Mianyang 621010, China*

[5] *State Key Laboratory of Metastable Materials Science & Technology and Key Laboratory for Microstructural Material Physics of Hebei Province, School of Science, Yanshan University, Qinhuangdao, 066004, People's Republic of China*

[6] *Department of Physics, Department of Materials Science and Engineering, and Department of Biomedical Engineering, City University of Hong Kong, Tat Chee Avenue, Kowloon, Hong Kong, China*

* Corresponding author: msm-liu@126.com (C. Liu)

Abstract

Micro-airflow sensing requires high sensitivity and mechanical robustness, but conventional diaphragm- or cantilever-based fiber probes struggle to excel in both. Here, we report a T4 bacteriophage-inspired six-legged fiber-optic Fabry–Pérot (F-P) sensor. Six flexible tail fibers act as the elastic supporting legs, the baseplate serves as the F-P reflector, and the head acts as a wind catcher. The entire probe is printed in a single step onto a fiber end face using femtosecond two-photon polymerization. The optimized cavity length is 22 μm, the tail-fiber width and thickness are both 3 μm, and the included angles are 60° and 85 °, respectively. The sensor responds linearly from 4 to 355 sccm, with a sensitivity of −0.099 nm/sccm, a detection limit of 4 sccm, and a resolution of 0.002 sccm. The response and recovery times are 8 ms and 3 ms, respectively. After a 15 μm compression impact, the probe recovers elastically, whereas a conventional cantilever deforms irreversibly. The load-sharing design of six legs combines high sensitivity with high toughness, and the results reveal a new route for micro-flow metering, breath monitoring, and turbulence warning.

Keywords: T4 bacteriophage; biomimetic structure; fiber-optic sensor; Fabry–Pérot interference; micro-airflow detection; two-photon polymerization

1. Introduction

Accurate measurement of micro-airflow, defined here as a mass flow below 1 L/min, is increasingly demanded in semiconductor processing, fuel cells, respiratory monitoring, and aviation safety [1]. Although thermal flowmeters offer high sensitivity and fast response, they consume considerable power and are sensitive to gas species and ambient temperature [2]. Piezoresistive MEMS sensors inspired by insect hairs exhibit improved response to weak flows through the lever effect of slender hairs [3-6], but they require electrical wiring and suffer from poor electromagnetic compatibility. Variable-area rotameters are simple and cover a wide range, but they are bulky and have a high lower detection limit [7]. In this respect, optical fiber sensors provide an excellent alternative because of their immunity to electromagnetic interference, intrinsic safety, and ease of miniaturization. Representative schemes include fiber loop ringdown [8], optical triangulation [9], and Fabry–Pérot (F-P) interference [10], [11]. Among them, the F-P interferometry offers a compact structure and high fringe contrast, making it the most promising for miniaturization. Existing F-P airflow probes mostly rely on polymer diaphragms or single cantilevers, but the diaphragms can be too stiff to deflect appreciably under a small pressure difference, while the cantilever suffers from stress concentration at its root and deforms plastically under overload, making it difficult to reconcile sensitivity and reliability.

Nature offers a paradigm that combines sensitivity with toughness. Insect filiform hairs amplify viscous drag into a rotation at the base through a slender lever and can perceive airflows of a few millimeters per second [3], [4]. A single hair is essentially a

cantilever. The T4 bacteriophage, in contrast, adopts a multi-support architecture composed of six tail fibers, a baseplate, and a head: the six tail fibers share the load and undergo large, reversible bending during infection [12-16], suggesting a new strategy for distributing joint stress and enhancing structural toughness. Integrating such three-dimensional architectures onto a fiber end face requires true 3D fabrication with submicrometer precision, which is exactly what femtosecond two-photon polymerization (TPP) provides [17-19]. TPP has already been used to produce microlenses, microcavities, and micro-force probes on fiber tips [20], [21]. However, to the best of our knowledge, the combination of a phage-mimetic multi-leg structure with F-P airflow sensing has not been reported.

In this work, a T4-phage-inspired optical fiber F-P micro-airflow sensor is designed and demonstrated. The tail fibers act as elastic supporting legs, the baseplate serves as the F-P reflector, and the head acts as a wind catcher. The six-legged probe is printed in a single step on the end face of a single-mode fiber. The cavity length, tail-fiber dimensions, and included angles are optimized using coupled fluid–structure interaction and interference simulations, and stress concentrations at the joints are eliminated by fillet rounding. The static sensitivity, detection limit, resolution, dynamic response, and temperature/humidity stability are characterized. The optimized sensor exhibits a linear response from 4 to 355 sccm, with a sensitivity of −0.099 nm/sccm, a detection limit of 4 sccm, a resolution of 0.002 sccm, and response/recovery times of 8 ms/3 ms. After a 15 μm compression impact, the probe fully and elastically recovers, showing markedly greater toughness than a conventional cantilever. The load-sharing

design reconciles high sensitivity with high toughness, offering a new route for micro-airflow detection.

2. Sensing principle

2.1 Sensing model

The T4 bacteriophage has six radiating tail fibers that withstand complex fluid environments, making it an ideal model for developing tough and sensitive biomimetic probes. Fig. 1(a) shows a transmission electron microscopy (TEM) image of the T4 bacteriophage, and its main structural components, including the head, tail tube, baseplate, and tail fibers, are shown in Fig. 1(b). The biomimetic sensing model built on this architecture is shown in Fig. 1(c) [12], [13]. The tail fibers act as multiple supporting legs, the baseplate as the reflector, and the head as a wind catcher, forming an F-P cavity airflow sensor based on optical interference.

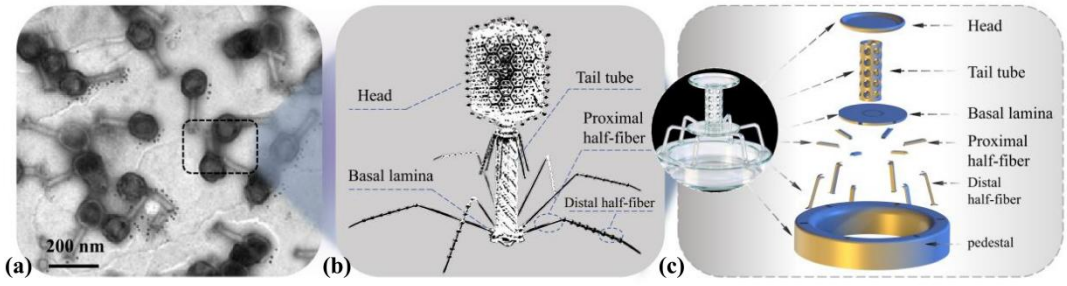


Fig. 1. T4 bacteriophage and the biomimetic sensing model: (a) TEM image of the T4 bacteriophage; (b) Main components; (c) Biomimetic micro-airflow sensing model.

2.2 Theoretical analysis

The sensing principle relies on F-P interference [10]. The airflow changes the cavity length, thereby shifting the interference spectrum. The cavity is a composite structure containing several reflecting surfaces, but only the length of the FP1 cavity formed by the fiber end face and the lower surface of the baseplate is modulated by the airflow. In addition, light is strongly attenuated in the polymer, so the reflected intensity is very weak. Therefore, only the FP1 cavity is analyzed, and its interference intensity can be expressed as

$$I=I_1+I_2+2\sqrt{I_1 I_2}\cos(\frac{4\pi nL}{\lambda}), \quad (1)$$

where I_1 and I_2 are the reflected intensities from the fiber end face and the baseplate, respectively, λ is the wavelength of the incident light, and n is the refractive index of the medium in the cavity. The phase at the interference minima satisfies

$$\frac{4nL}{\lambda_m}=(2m+1)\pi, \quad (2)$$

where m is the interference order and λ_m is the wavelength of the m^{th} interference minimum. The free spectral range (FSR) is given by

$$FSR=\frac{\lambda^2}{2nL}. \quad (3)$$

In addition, the mechanical properties of the probe depend on the intrinsic properties and geometry of the polymer. To accomplish high sensitivity, the fabrication parameters and geometry are systematically optimized as described below.

3. Materials and methods

3.1 Fabrication process and structural optimization

The fabrication process is illustrated in Fig. 2. The coating on a commercial single-

mode fiber (125 μm in diameter) was removed (a), and a flat end face was obtained with a fiber cleaver (b). The fiber was inserted into a homemade glass fixture with its end face facing upward (c), and the fixture was fixed on a vacuum chuck (d). Photoresist (ATE-DIP, Magie-Nano Technology Co., Ltd., Yantai, China) was dropped onto the glass slide to immerse the fiber end face (e), and the chuck was mounted on a precise three-dimensional translation stage (f). The vacuum chamber with a femtosecond 3D printer (PROME-Uni, Yantai Moji Nano Technology Co., Ltd., Yantai, China) was then closed and kept at 25 °C and 40% relative humidity (g). The stage was adjusted by a PC so that the laser was focused 10 μm below the fiber end face (h), and the pre-optimized program was executed (i). After printing, the sample was sequentially developed in PGMEA (60 s), isopropanol (40 s), and n-hexane (15 s) to remove uncured resist, then dried in air for about 5 min (j). It was taken out and further dried for 10 min to complete the fabrication (k).

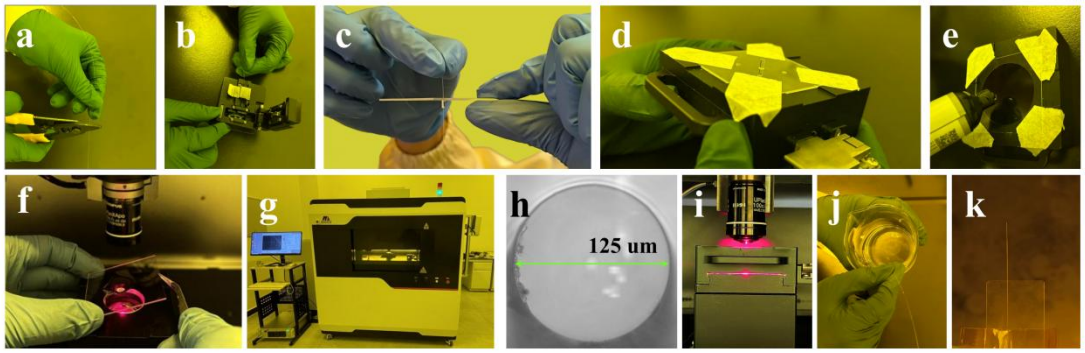


Fig. 2. Fabrication process of the T4-phage-inspired micro-airflow sensor.

In this process, the femtosecond-laser parameters in step (g) governed the probe

quality and were therefore studied systematically. The standard parameters provided by the manufacturer were adopted, including the ultrahigh-speed mode, sampling rate of 10,000 points/s, point spacing of 0.025 μm, line dwell time of 5 ms, layer dwell time of 100 ms, interface position of 100 μm, 100× objective, slice thickness of 0.1 μm, and laser wavelength of 550 nm. Because laser power strongly affected material properties, polymerization was compared across 5%–100% of the total power at a fixed total power of 500 mW (Fig. 3). No polymerization occurred at 5%–25%. Polymerization started at 30%, became progressively stronger from 35% to 85%, and then entered a violent boiling phase of the resist at 90%–100%.

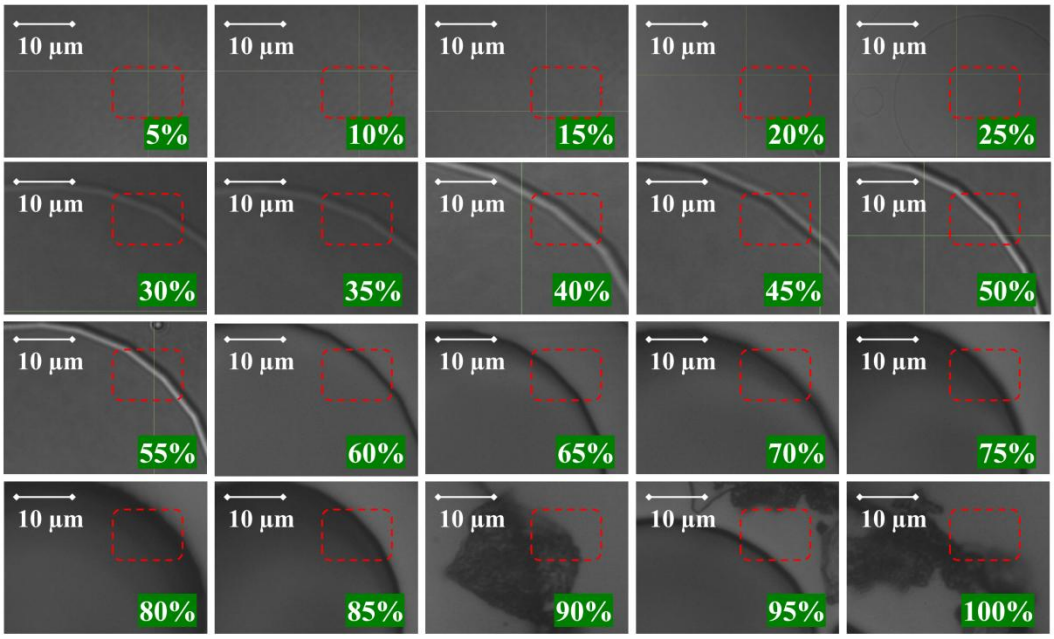


Fig. 3. Polymerization quality of the photoresist as a function of laser power.

The refractive index (n), polymerization conversion (PC), crosslink density (CD), material density (MD), and voxel size (VS) of the polymerized material are plotted

against laser power in Fig. 4. All the parameters increase logarithmically with power and then saturate. The refractive index of the single-mode fiber is about 1.45 [22], [23]. Since the fringe contrast increases as the refractive indices of the two F-P reflectors approach each other, 50% (500 mW) was selected. At this power, the resist is fully polymerized, and its refractive index differs from that of the fiber core by less than 0.2. The mechanical parameters of the material are: density = 1,503 kg/m³, Young's modulus = 2.01 GPa, and Poisson's ratio = 0.42.

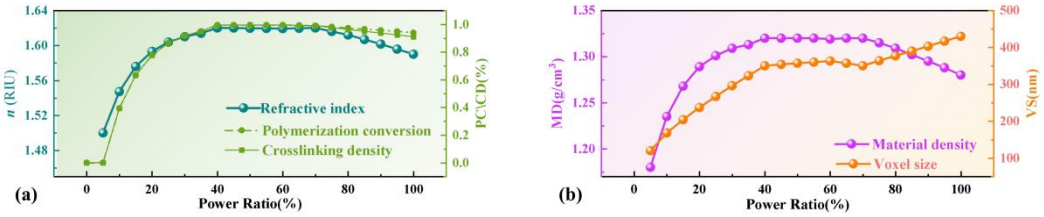


Fig. 4. Material parameters of the polymer as a function of laser power: (a) n, PC and CD; (b) CD and MD.

3.2 Biomimetic model design

Five initial biomimetic models were designed based on the T4 bacteriophage structure (Fig. 5). Model E most closely resembles the T4 morphology, and its tail fibers provide more flexible support and better airflow sensing, so model E was selected. However, its interference spectrum was not sufficiently pronounced because it was primarily determined by the F-P cavity length. The distance between the fiber end face and the baseplate was therefore further optimized.

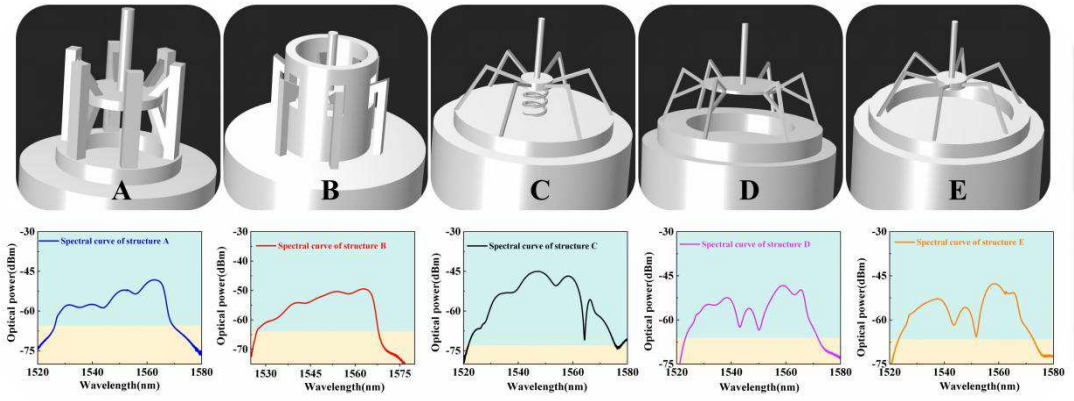


Fig. 5. Five initial sensing models designed from the T4 bacteriophage structure.

3.3 F-P cavity length optimization

To obtain a more pronounced interference pattern, the F-P cavity length was optimized in the range of 16–38 μm (Fig. 6(a)). An interference model of the fiber end face and the baseplate was constructed in COMSOL (Fig. 6(b)). The simulated electric-field distribution is shown in Fig. 6(c), where $|E_1|$ is the amplitude of the forward-propagating wave alone, without considering its coherent superposition with the backward reflected wave, while $|E_{total}|$ is the magnitude of the total electric field formed by the interference between the forward and backward waves inside the cavity. The $|E_{total}|$ distributions for different cavity lengths are compared in Fig. 6(d), and the corresponding interference spectra are shown in Fig. 6(e) and (f); at L = 22 μm, the spectrum exhibits high fringe contrast and a large free spectral range.

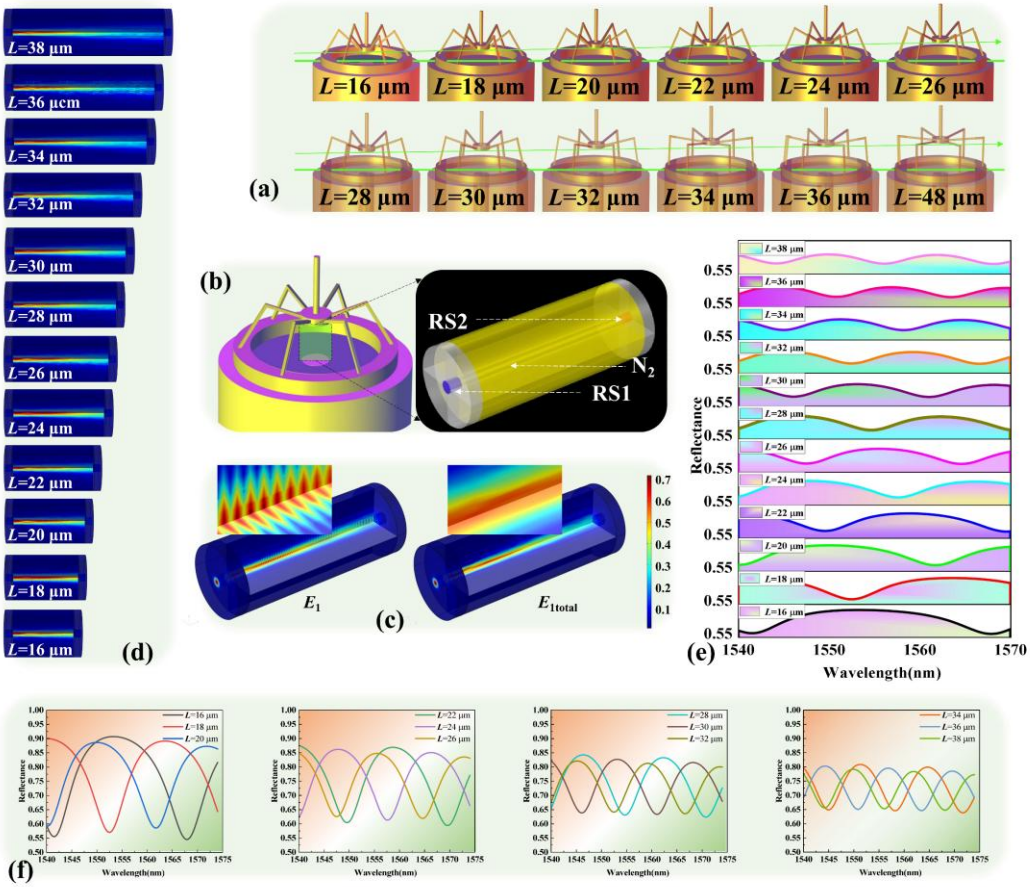


Fig. 6. Interference characteristics for different cavity lengths: (a) 3D model comparison (16–38 μm); (b) F-P simulation model; (c) electric-field distribution; (d) total electric field for different L; (e) interference spectra; (f) magnified spectra.

3.4 Tail tube optimization

To evaluate the elastic recovery of the biomimetic structures, four elastic probes were fabricated on fiber end faces by the same process and subjected to a rigid impact test (Fig. 7). Structures F and G were previously reported biomimetic cantilevers [20], [21], whereas H and I were T4-phage-inspired structures with tail tubes of different diameters. Driven by the motor of a fiber fusion splicer (80S, Fujikura, Tokyo, Japan), the four probes were pressed against a single-mode fiber end face with the same

compression ΔX = 15 μm. Structure F deformed irreversibly. Both the head and the cantilever of G deformed irreversibly. H recovered, but its tail tube tilted slightly. Only structure I recovered completely after impact.

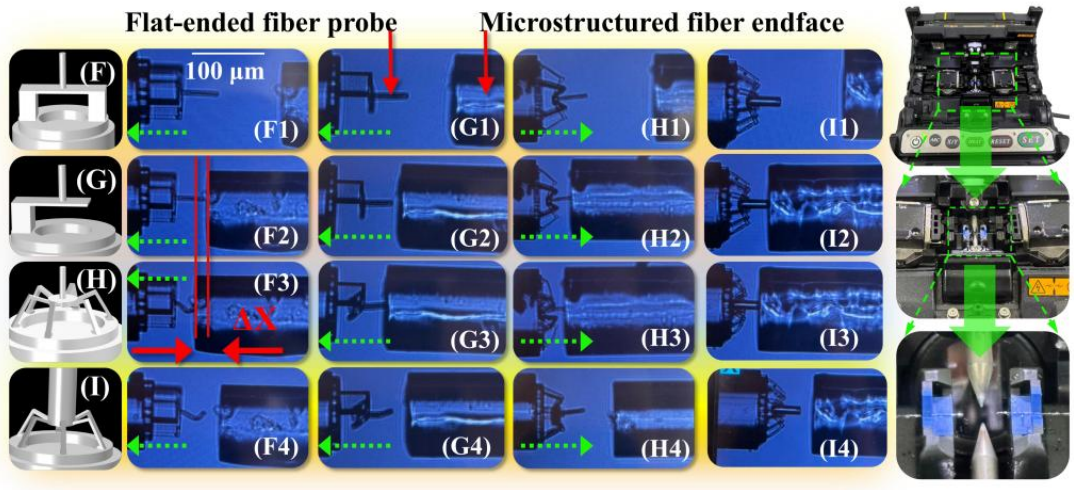


Fig. 7. Elastic recovery of the T4-phage-inspired structures compared with previously reported cantilevers.

The impact test shows that structure I has a stronger recovery capability than H, because the larger tail-tube radius increases the loaded area. The reflective area also increases, enhancing reflected intensity and interference. As shown in Fig. 8, thickening the tail tube optimizes the interference spectrum, and the longitudinal displacement of the tail tube under the same flow increases, thereby improving sensitivity.

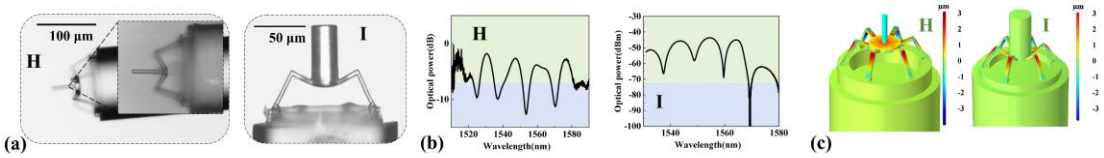


Fig. 8. Comparison of probes H and I: (a) Optical micrographs; (b) Interference spectra; (c) Fluid–structure interaction simulation of the displacement under 10 sccm N_2.

Although the optical and mechanical performance of structure I has improved, the tail tube-to-tail-fiber mass ratio is too large, causing the tail fibers to bear excessive load when the probe is placed horizontally. The tail-fiber structure was therefore further optimized, and seven designs were proposed (Fig. 9). Design 7, with a lighter tail tube and a larger fringe contrast and free spectral range, was therefore selected.

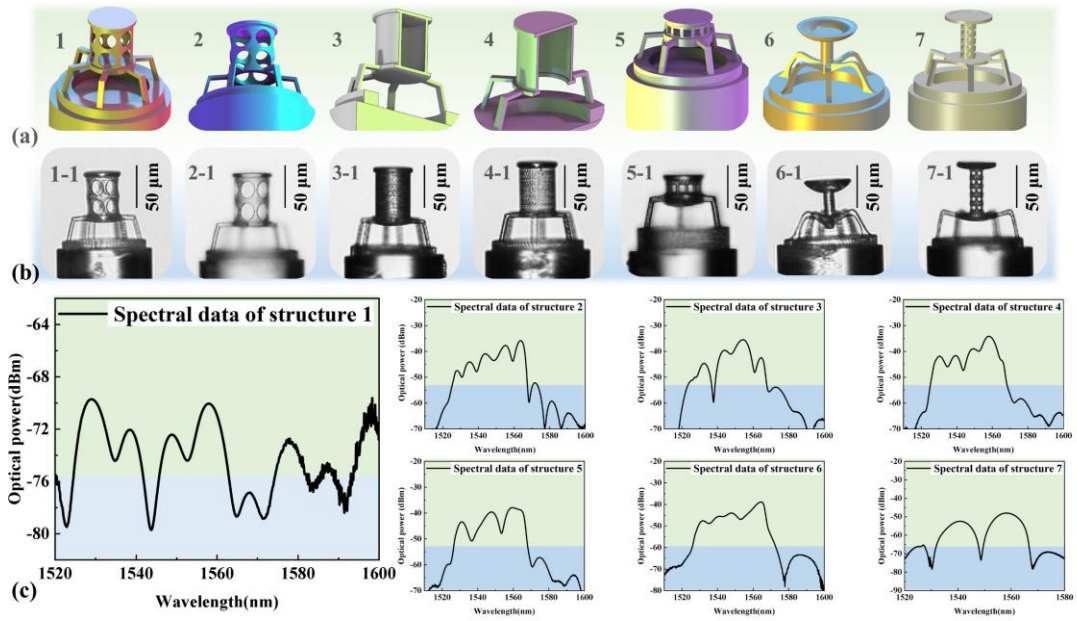


Fig. 9. Seven tail-tube designs derived from structure I: (a) 3D models; (b) Optical micrographs of the printed structures; (c) Interference spectra.

The geometric parameters of structure 7 are defined in Fig. 10(a): cavity length L = 22 μm; tail-fiber width L_1 and thickness L_2; head/baseplate thickness L_3 = 3 μm and

diameter L_4 = 30 μm; distal and proximal half-fiber lengths = L_5 and L_6; angle between the distal half-fiber and the horizontal plane = θ_1; angle between the distal and proximal half-fibers = θ_2; base thickness L_7 = 10 μm, which enlarges the contact area with the single-mode fiber and improves adhesion; and tail-tube diameter d = 20 μm. To reduce the probe mass, the tail tube was hollowed and perforated. The holes are 4 μm in diameter, with six evenly distributed in each layer, and the layer spacing is 1.5 μm. Perforation also facilitates the drainage of uncured developer. The stress distribution obtained from the fluid–structure interaction simulation is shown in Fig. 10(b). A stress concentration was evident at the joints, so the joints were rounded with a fillet radius of 3 μm. The optimized stress distribution in Fig. 10(c) shows that the stress concentration has essentially been eliminated.

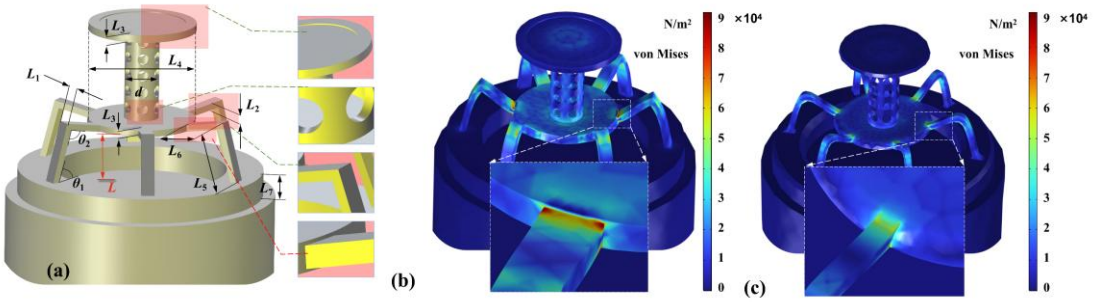


Fig. 10. Structure 7: (a) Definition of structural parameters; (b) Fluid–structure interaction stress distribution; (c) Stress distribution after joint rounding.

The tail-tube length is further optimized (Fig. 11). The experiments show that the head, acting as a secondary reflector of the composite F-P cavity, slightly affects the interference spectrum through its distance to the baseplate. When the tail tube has a

five-layer circular-hole structure (structure N), the interference peaks are the most regular, and structure N is therefore selected.

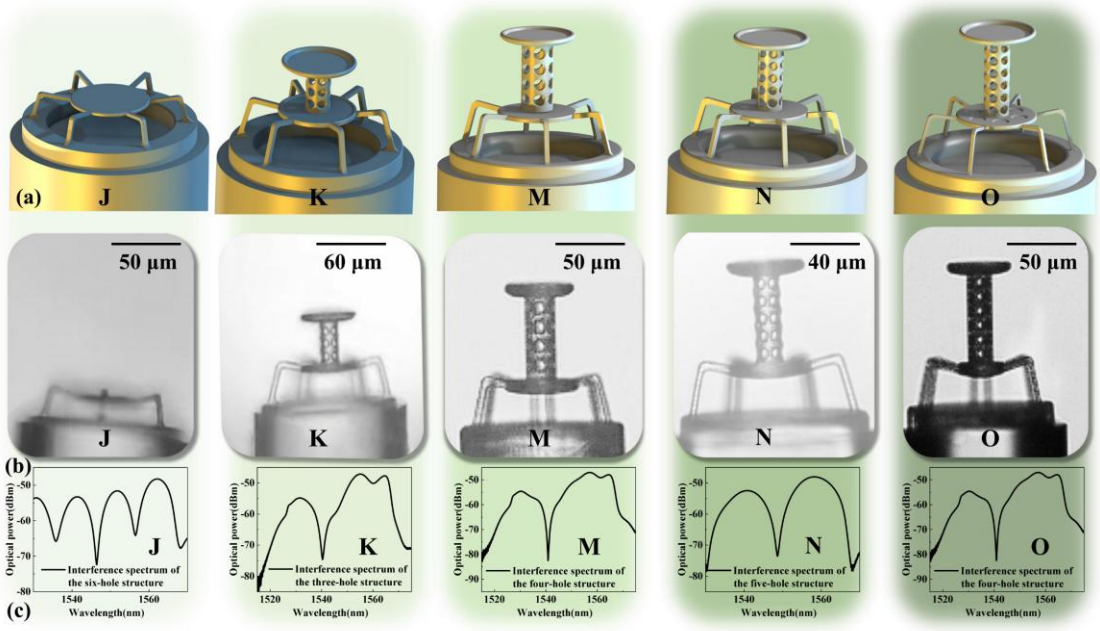


Fig. 11. Structures with five different tail-tube lengths: (a) 3D models; (b) Optical micrographs; (c) interference spectra.

3.5 Tail fibers optimization

The dimensions and angles of the tail fibers are critical to the sensitivity. Once the cavity length, baseplate diameter, and angles θ_1 and θ_2 are fixed, the proximal and distal half-fiber lengths, L6 and L5, are determined and therefore not analyzed separately. The combination of angles and cross-sectional dimensions is the focus. θ_1 and θ_2 are strongly coupled with respect to sensitivity, so they are optimized jointly by constructing a three-dimensional color-mapped surface (Fig. 12(a)), with θ_1 (40°–80°) and θ_2 (80°–120°) as the horizontal axes and the axial displacement of the baseplate as

the vertical axis. The results show that the sensitivity is high at $\theta_1 = 60°$ and $\theta_2 = 85°$. Similarly, the tail-fiber width L_1 (1–10 μm) and thickness L_2 (1–6 μm) are strongly coupled (Fig. 12(b)): thinner fibers give higher sensitivity, but, limited by the printing process, the probe collapses when both dimensions are smaller than 2 μm (inset of Fig. 12(b)). Taking both effects into account, $L_1 = L_2 = 3$ μm was chosen.

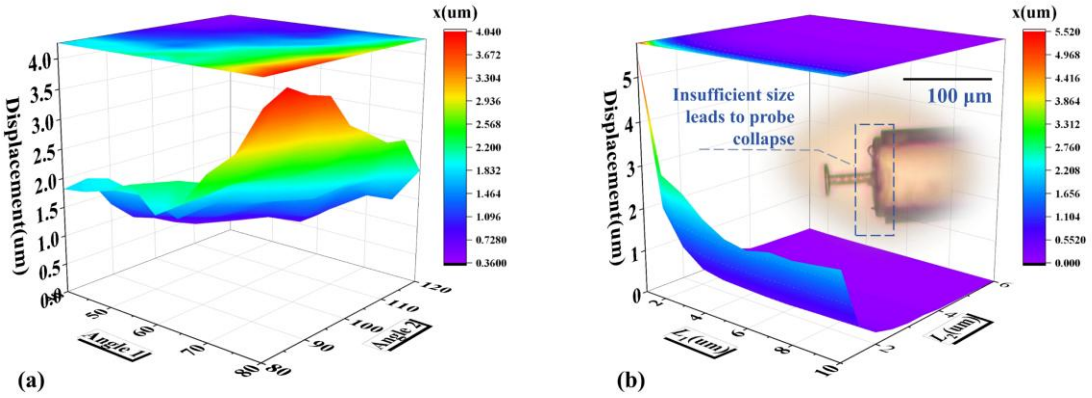


Fig. 12. Axial displacement of the baseplate versus structural parameters under a flow of 150 sccm: (a) θ_1 and θ_2; (b) L_1 and L_2.

In summary, the optimized structural parameters are L = 22 μm, $L_1 = L_2 = 3$ μm, $L_3 = 3$ μm, $L_4 = 30$ μm, $\theta_1 = 60°$, $\theta_2 = 85°$, $L_7 = 10$ μm and d = 20 μm. The probe fabricated by the process in Section 3.1 is shown in Fig. 13, and its actual morphology agrees well with the design.

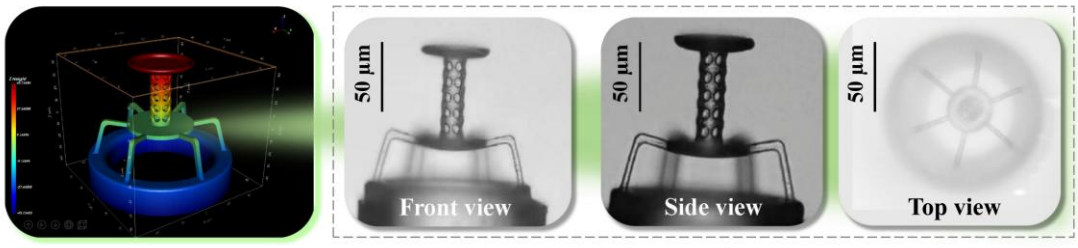


Fig. 13. Optical micrographs (three views) of the final T4-phage-inspired micro-airflow sensor.

3.6 Sensor performance

During testing, the probe frequently collided with the gas outlet and detached. A capillary tube (inner diameter 290 µm, outer diameter 410 µm) was therefore mounted outside the probe for protection (Fig. 14(a)). A fluid–structure interaction model was established in COMSOL (Fig. 14(b)). The capillary and the single-mode fiber were both set as silica (density 2700 kg/m³, Young's modulus 73 GPa, Poisson's ratio 0.17). The probe material followed Section 3.1 (density 1503 kg/m³, Young's modulus 2.01 GPa, Poisson's ratio 0.42), and the inlet used a standard flow rate (SCCM) defined at 1 atm and 298.15 K, with a mean molar mass of 0.02897 kg/mol for nitrogen. The sensing principle is illustrated in Fig. 14(c). The mesh quality was evaluated with the skewness metric. Most elements have high skewness, satisfying the accuracy and stability requirements of the numerical solution (Fig. 14(d)).

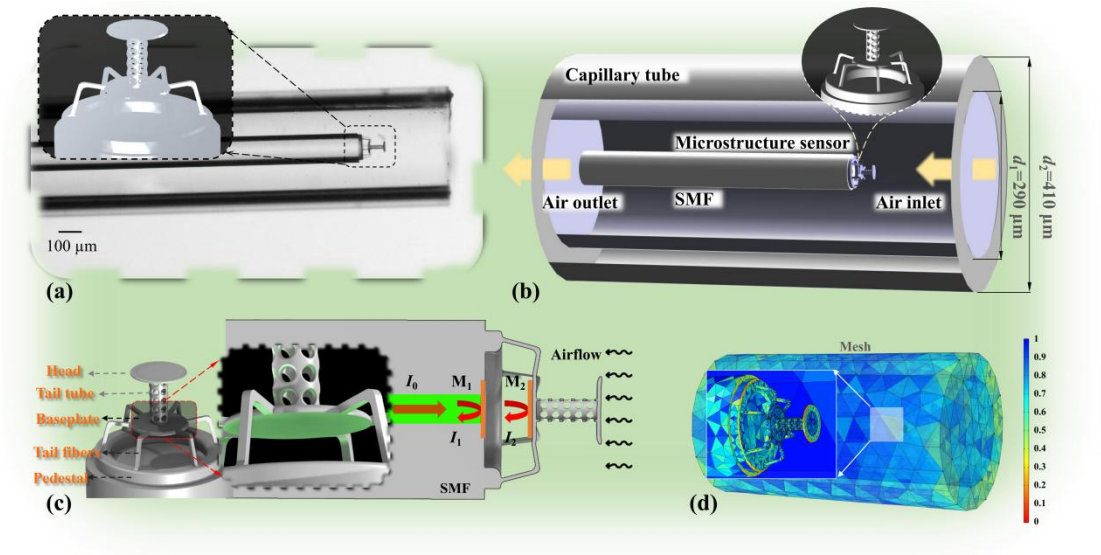


Fig. 14. Packaging and simulation model: (a) Optical micrograph of the sensor with the capillary; (b) Simulation model for the airflow test; (c) Schematic of the sensing principle; (d) Skewness-based mesh quality evaluation.

Fig. 15(a) shows the distributions of gas velocity and axial displacement at an inlet flow of 100 sccm. Deformation is pronounced, with a displacement amplitude of about 1 μm. Fig. 15(b) presents the stress amplitude. Stress concentrates in the region where the tail fibers join the baseplate, and the inset shows a magnified view together with a threshold-filtered contour (regions with more than 50% of the maximum stress). Fig. 15(c) shows the strain-tensor amplitude, with the corresponding magnified and threshold-filtered views in the inset. Fig. 15(d) shows the pressure distribution: pressure concentrates at the head, reaches about 150 Pa, and decays gradually along the axial direction.

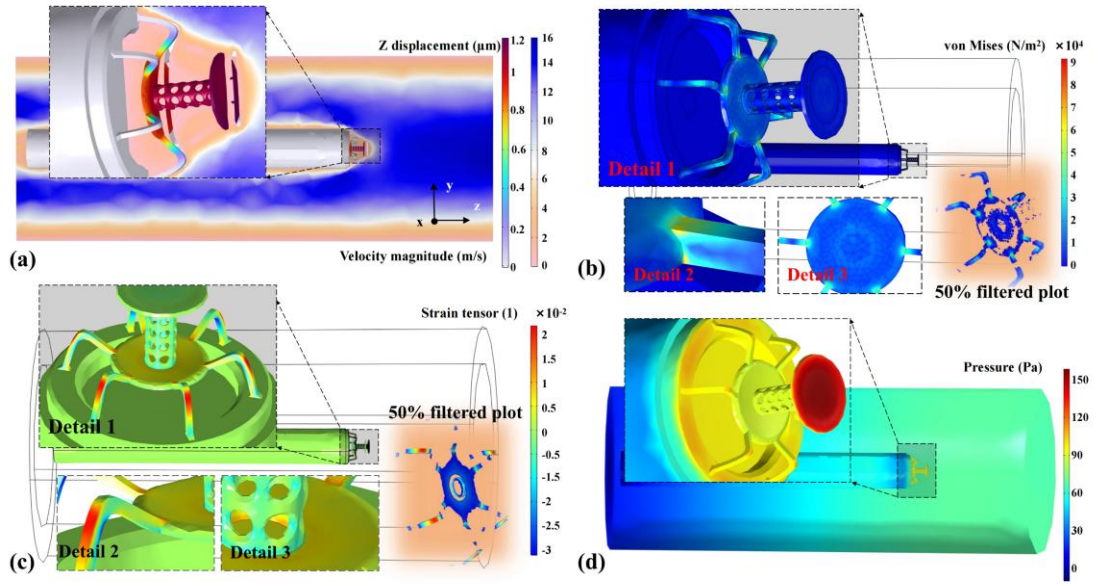


Fig. 15. Simulation results at 100 sccm N_2: (a) Flow velocity and axial displacement; (b) Stress distribution; (c) ZZ component of the strain tensor; (d) Pressure distribution in the laminar flow.

Transient simulations were also performed. The inlet nitrogen flow increases linearly with time, $Q_g = t$ (sccm), as shown in Fig. 16(a). The inset shows the velocity isosurface at 90 sccm. Under the airflow load, the baseplate displaces axially, and the displacement–time curve is S-shaped (Fig. 16(b)). It increases slowly at first, then rises rapidly and finally saturates. This behavior originates from the elastic deformation of the tail fibers, which obeys the constitutive relation of elasticity. The linear detection limit of the sensor is therefore estimated at about 800 sccm. When the inlet flow exceeds 1,100 sccm, the simulation diverges due to excessive mesh deformation (inset of Fig. 16), and no valid solution can be obtained. The transient stress and strain curves at monitoring points P1–P4 are shown in Fig. 16(c) and (d), respectively. Both are

parabolic and begin to decrease after about 800 s (corresponding to 800 sccm), indicating that the airflow force exceeds the probe's elastic limit, consistent with Fig. 16(b).

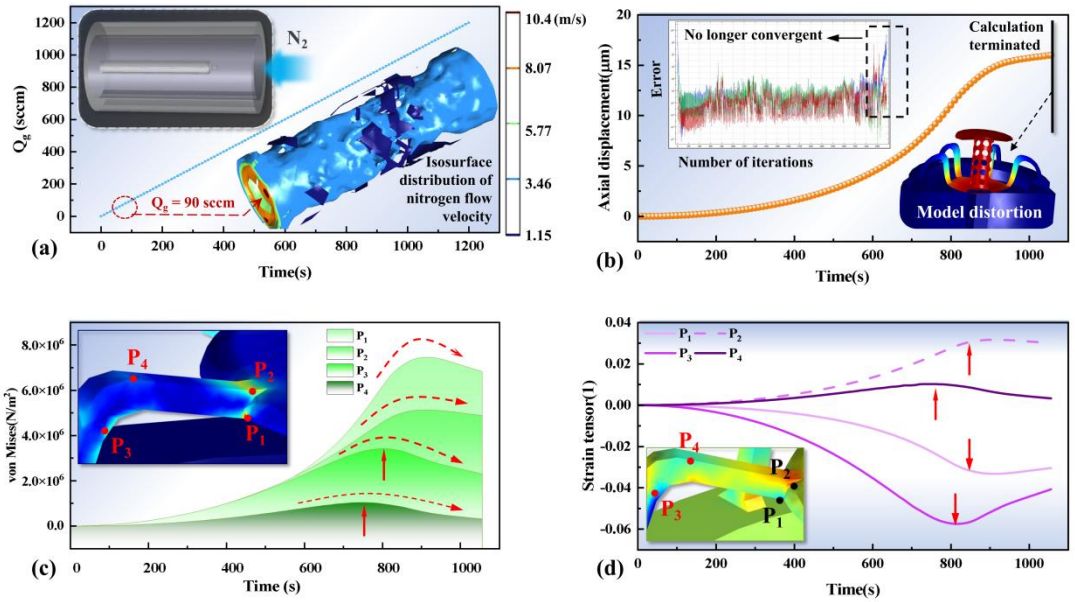


Fig. 16. Transient simulation results: (a) Time-varying inlet nitrogen flow; (b) Axial displacement of the baseplate; (c) Stress and (d) Strain at points P1–P4.

3.7 Test system and procedures

The test procedure is shown in Fig. 17. Procedure I measures hysteresis, repeatability, response time, and recovery time, while procedure II measures the detection limit, resolution, and temperature/humidity stability.

Procedure I: a distributed-feedback laser (1550 nm, DFB15TK, Thorlabs, Shanghai, China) was used as the source (A) and split into two paths by a 1×2 fiber coupler (C). One path was connected to the sensor (G) housed in the capillary and inserted into the

gas conduit (H_3). H_3 was supplied with nitrogen from a cylinder (H_1, YQD-370B, Linhai Baohua Instrument Co., Ltd., Linhai, China) through a gas flowmeter (H_2, ACU30FC-LCMX300C, Beijing ACCUFLOW Technology Co., Ltd., Beijing, China). The flow meter was combined with a Burkert 2873 direct-acting normally closed proportional solenoid valve (with an 8605 signal controller) to modulate the flow, producing discrete stepwise increasing–decreasing cycles with a time resolution of 25 ms over 200–260 sccm, with 0.01 s on and 0.015 s off. The other path was connected to a germanium photodetector (D, PDA30B2, Thorlabs, Newton, MA, USA) and then to a data acquisition card (E, USB-6009, National Instruments, Austin, TX, USA), which converted the intensity variation into a voltage signal transmitted in real time to a PC.

Procedure II: A broadband source (B, Luceo, Tokyo, Japan) was used, and after the coupler (C), one path was connected to the sensor (G), which was placed in a humidity controller (J, SV-202B-3, Guangzhou SIEVAL Electronics Co., Ltd., Guangzhou, China) for humidity stability, in a temperature controller (K, HYHG-II-72, Shanghai Yuejin Medical Instrument Co., Ltd., Shanghai, China) for temperature stability, and in the gas conduit (H_3) for airflow sensitivity. The other path was connected to an optical spectrum analyzer (I, AQ6370D, Yokogawa, Tokyo, Japan) to record the spectral variation.

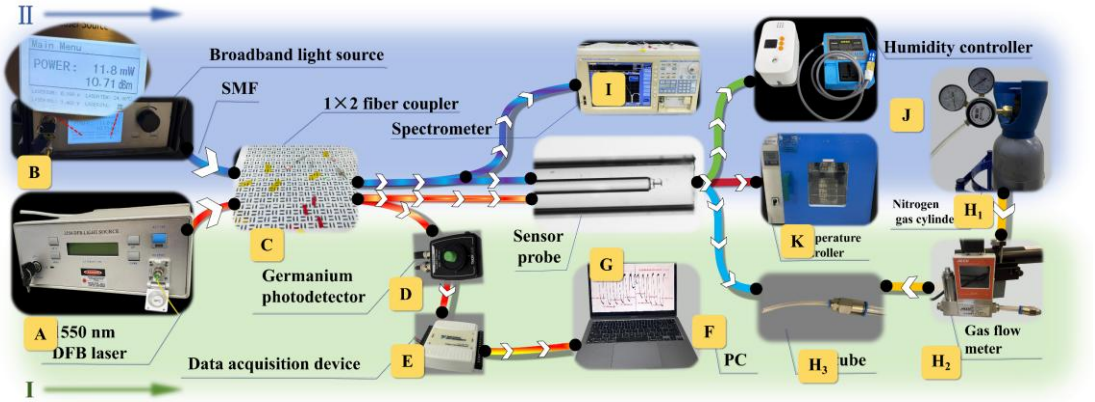


Fig. 17. Schematic of the sensor test system.

Data availability

The experimental data supporting the conclusions of this study are available from the corresponding author upon reasonable request.

4. Results

4.1 Static airflow response

At 20 °C, 50% RH and standard atmospheric pressure, the airflow response spectra were acquired using procedure II (Fig. 18). The interference spectrum starts to blueshift when the nitrogen flow exceeds 3 sccm (Fig. 18(a)). The blueshift persists from 10 to 14 sccm (Fig. 18(b)). Between 15 and 355 sccm, the shift increases with flow (Fig. 18(c) and (d)), while from 455 to 1,455 sccm, the spectrum still blueshifts, but the magnitude decreases with increasing flow (Fig. 18(e)).

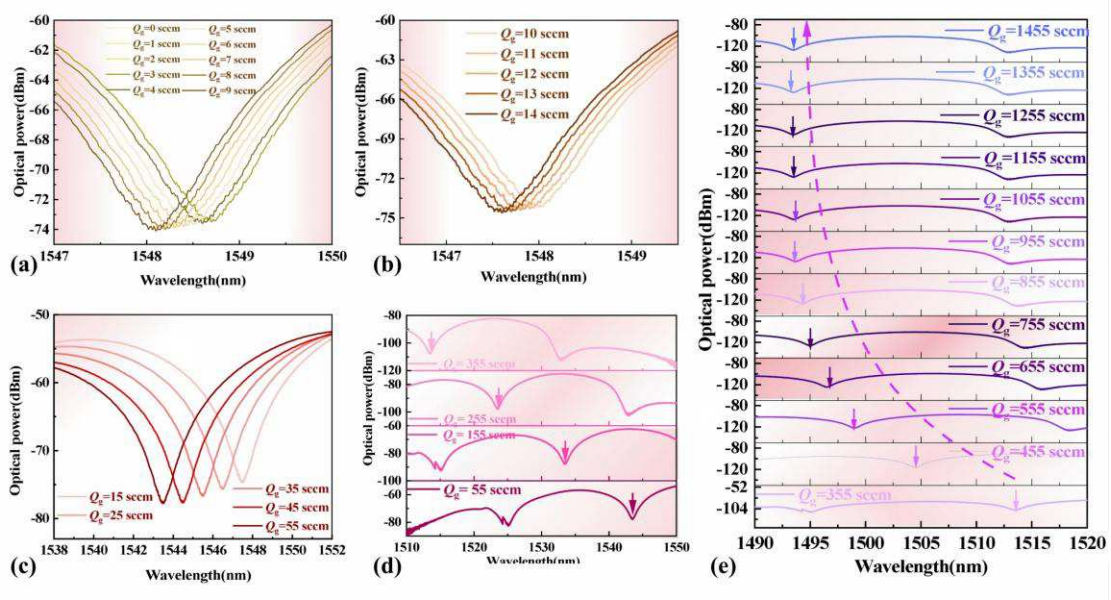


Fig. 18. Shift of the interference spectra at different nitrogen flows: (a)–(e) Corresponding to different flow intervals within 0–1,455 sccm.

The shifts of the interference minima in Fig. 18 are fitted piecewise linearly, and the overall curve is S-shaped (Fig. 19(a)), consistent with the simulation trend. In the 0–4 sccm interval (Fig. 19(b)), the average sensitivity is −0.028 nm/sccm with R^2 = 92.31%. The linearity is poor, so this interval is not used as the effective range, and the detection limit is set to 4 sccm. For the 4–14, 15–55, and 55–355 sccm intervals, the average sensitivities are −0.0993, −0.103, and −0.097 nm/sccm, with R^2 of 99.65%, 99.72%, and 99.33%, respectively. In the 355–755 sccm interval, the average sensitivity decreases to −0.0450 nm/sccm (R^2 = 85.94%), and beyond 755 sccm, the spectrum no longer shifts significantly.

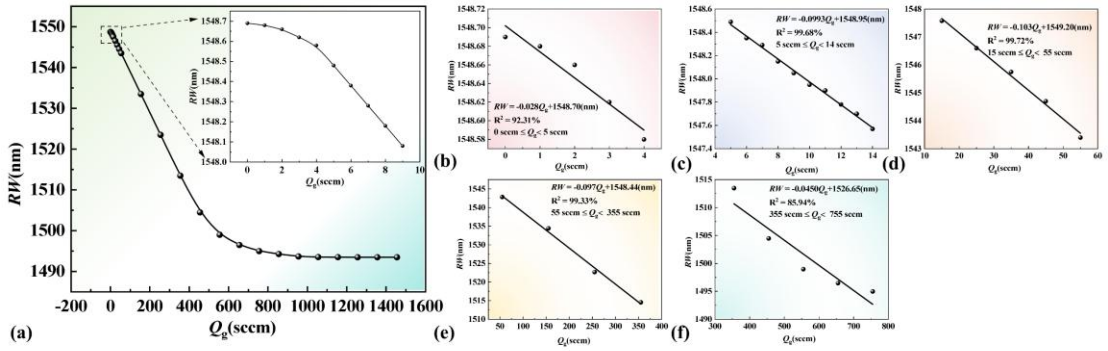


Fig. 19. Piecewise linear fitting of the interference-minimum shift: (a) overall curve; (b)–(f) individual flow intervals.

4.2 Dynamic airflow response

At 20 °C, 50% RH and standard atmospheric pressure, the dynamic response was measured using procedure I, and about 1000 increasing–decreasing cycles were completed within 200 s (Fig. 20(a)). The output voltage decreases as the flow increases and increases as the flow decreases. One cycle is magnified for analysis (Fig. 20(b)), and the times corresponding to 90% of the total voltage change are taken as the response time (tres) and recovery time (trec). The point-density distribution of nearly 1000 cycles (Fig. 20(c)) gives a response time of 8 ms and a recovery time of 3 ms. When the flow is cycled between 200 and 260 sccm, the output voltage is fitted linearly against flow (Fig. 20(d)). The sensitivities of the increasing and decreasing branches are essentially the same, about 0.001 V/sccm.

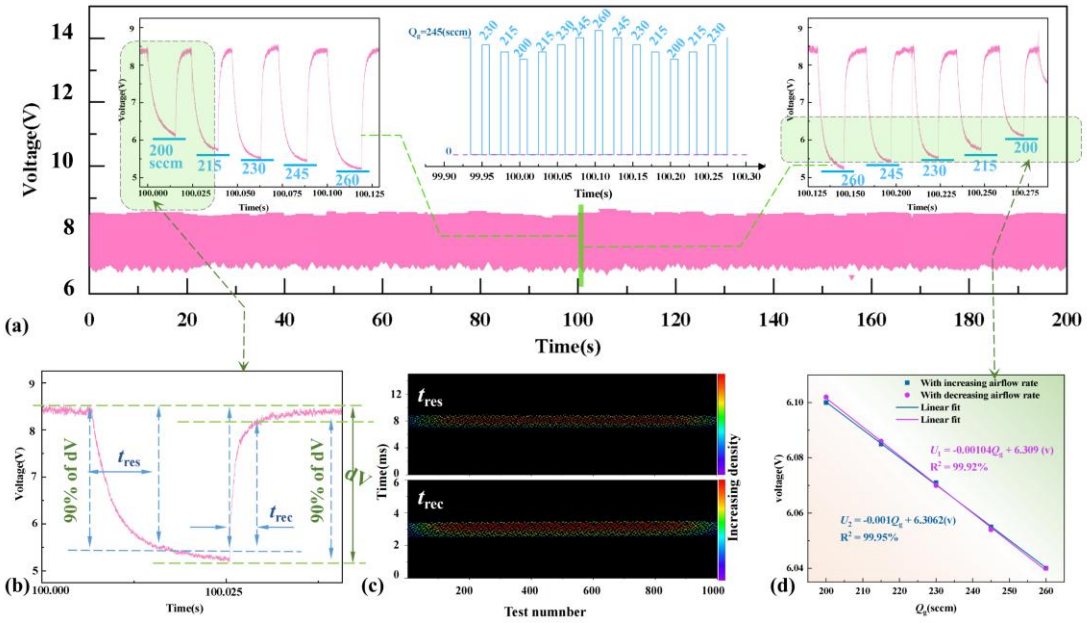


Fig. 20. Dynamic response during 200–260 sccm cycling: (a) Output voltage over 200 s (inset: flow input and the 100–100.275 s window); (b) Magnified view of 100–100.04 s; (c) Point-density distribution of response/recovery times over 1,000 cycles; (d) Output voltage versus flow for a single cycle.

4.3 Temperature stability

Temperature tests were carried out from 10 to 220 °C in both heating and cooling modes (Fig. 21). During heating, the spectrum redshifts, with an average temperature sensitivity of 0.007 nm/°C (R^2 = 99.99%), while during cooling, it blueshifts, with an average sensitivity of 0.008 nm/°C (R^2 = 86.85%).

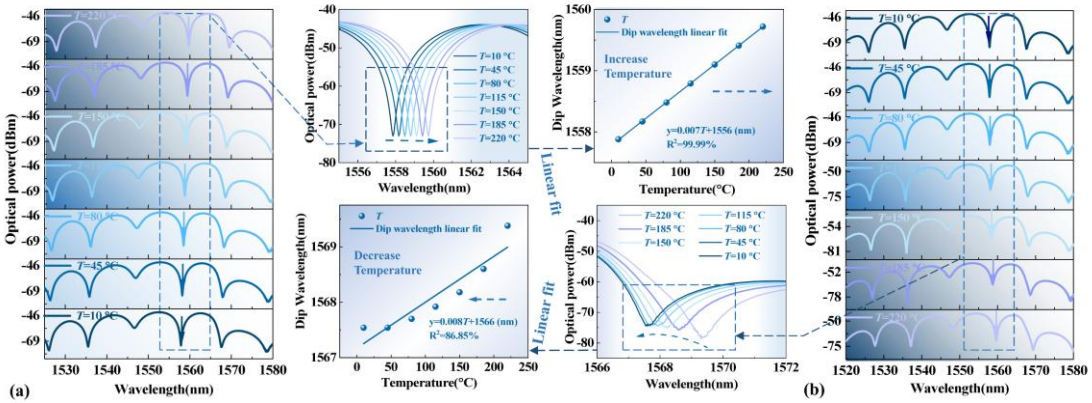


Fig. 21. Temperature response from 10 to 220 °C: (a) Heating; (b) Cooling.

4.4 Humidity stability

Humidity tests were carried out from 40% to 90% RH in both humidification and dehumidification modes (Fig. 22). During humidification, the spectrum redshifts, with an average relative-humidity sensitivity of 0.012 nm/%RH (R^2 = 96.05%). During dehumidification, it blueshifts, with an average sensitivity of 0.0026 nm/%RH (R^2 = 99.77%).

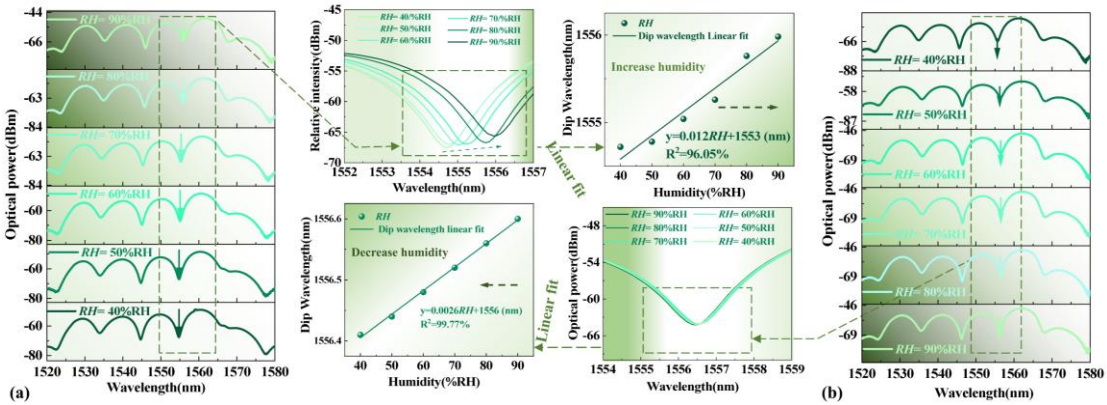


Fig. 22. Humidity response from 40% to 90% RH: (a) Humidification; (b) Dehumidification.

5. Discussion

The effective detection range of the sensor is 4–355 sccm. Beyond this range, degraded linearity and reduced sensitivity prevent the output from faithfully representing the actual flow. When the flow exceeds 755 sccm, the interference minimum hardly shifts because the airflow force exceeds the elastic limit of the microstructure, and the tail fibers can no longer produce an equivalent displacement to modulate the cavity length, consistent with the simulations. With the optical spectrum analyzer's 0.02 nm resolution, the sensor's airflow resolution is 0.002 sccm. The response and recovery times of 8 ms and 3 ms depend on the probe structure and material stiffness as well as on the transient behavior of the flow. The force acting on the probe is not an ideal step signal and requires a buffer period to reach equilibrium. In the cycling test, the sensor shows good stability and low hysteresis due to its phage-mimetic structure. In the temperature and humidity tests, the temperature sensitivity is below 0.01 nm/°C. The slightly lower sensitivity during cooling stems from irreversible deformation caused by the high temperature in the heating stage. The humidity sensitivity does not exceed 0.012 nm/%RH. The probe absorbs moisture as humidity rises, and this process is poorly reversible, so the interference minimum hardly shifts during dehumidification.

Table 1 compares the present sensor with five representative airflow sensors. Because the reported devices use volumetric flow (m^3/h, slpm), flow velocity (m/s, mm/s), or mass flow (sccm), all the values are converted to a common basis using 1 sccm ≈ 1 mL/min and 1 m^3/h ≈ 16667 sccm. The lower limit of the present sensor (4

sccm) is more than three orders of magnitude lower than that of the variable-area rotameter (1 m^3/h). Its sensitivity (−0.099 nm/sccm) is about four orders of magnitude higher after conversion, and its resolution (0.002 sccm) and response/recovery times (8 ms/3 ms) are also better than those of the other schemes. This advantage originates from the load-sharing biomimetic architecture: the six tail fibers distribute the aerodynamic force so that each fiber carries about F/6, producing a sufficient axial displacement even at very low flow while spreading the joint stress, reconciling high sensitivity with high toughness. The temperature- and humidity-induced drifts (0.007 nm/°C and 0.012 nm/%RH) can be further suppressed by reference-cavity compensation or dual-parameter demodulation [24].

Table 1. Comparison of gas flow sensors.

Ref.	Sensing mechanism	Range	Sensitivity	Resolution	Response/recovery time
[7]	Variable-area rotameter	1–6.5 m^3/h	0.22 nm/($m^3 \cdot h^{-1}$)	0.9 m^3/h	<1 s
[8]	Fiber loop ringdown	5–22.5 slpm	0.0016 dB/slpm	2.5 slpm	≈1 s
[9]	Optical triangulation	0–90 mm/s	0.7732 μm/(mm/s)	/	/
[6]	Piezoresistive	1–50 L/min	/	0.053 m/s	1.7 s/3.4 s

	(insect-hair mimetic)				
[1]	Piezoresistive MEMS	0–±5 m/s	1.36 mV/(m·s^{-3})	0.5 mL/s	24.1 ms/36.14 ms
This work	T4-phage-inspired F-P cavity	4–355 sccm	0.099 nm/sccm	0.002 sccm	8 ms/3 ms

6. Conclusion

Inspired by the "six legs–baseplate–head" architecture of T4 bacteriophage, a biomimetic F-P micro-airflow sensor is fabricated in a single step on the fiber end face using femtosecond two-photon polymerization. With six flexible tail fibers as elastic supporting legs and the baseplate as the reflector, the probe responds linearly from 4 to 355 sccm with a sensitivity of −0.099 nm/sccm, a detection limit of 4 sccm, a resolution of 0.002 sccm, and response/recovery times of 8 ms/3 ms. Moreover, it recovers fully and elastically after a 15 μm compression impact, demonstrating better toughness than a conventional cantilever. The load-sharing design combines high sensitivity with high toughness, providing a new strategy for micro-airflow detection.

Acknowledgements

This work was jointly supported by the Heilongjiang Provincial Natural Science Foundation of China [JJ2026YX0192] and City University of Hong Kong Donation

Research Grants [DON-RMG 9229021 and 9220061].

References

[1] 1. Liu, F. et al. Bio-inspired, sensitivity-enhanced, bi-directional airflow sensor for turbulence detection. *Nanoscale* **16**, 4299–4307 (2024).

[2] 2. Kuo, J. T. W. et al. Micromachined thermal flow sensors—a review. *Micromachines* **3**, 550–573 (2012).

[3] 3. Chen, N. et al. Design and characterization of artificial haircell sensor for flow sensing with ultrahigh velocity and angular sensitivity. *J. Microelectromech. Syst.* **16**, 999–1014 (2007).

[4] 4. Dijkstra, M. et al. Artificial sensory hairs based on the flow sensitive receptor hairs of crickets. *J. Micromech. Microeng.* **15**, S132–S138 (2005).

[5] 5. Casas, J. et al. Why do insects have such a high density of flow-sensing hairs? Insights from the hydromechanics of biomimetic MEMS sensors. *J. R. Soc. Interface* **7**, 1487–1495 (2010).

[6] 6. Shen, C. et al. Bioinspired ultrasensitive and flexible airflow sensor based on short carbon fiber network. *Adv. Mater. Technol.* **8**, 2200571 (2023).

[7] 7. Wang, P. et al. Research on a novel variable-area optical fiber gas flow sensor. *Sens. Actuators A Phys.* **221**, 29–32 (2015).

[8] 8. Alali, H. & Wang, C. Fiber loop ringdown gas flow sensors. *Meas. Sci. Technol.* **25**, 115102 (2014).

[9] 9. Xiong, H. et al. All-optical airflow sensor enables simultaneous speed and

direction measurement. *Opt. Express* **27**, 20734 (2019).

[10] 10. Islam, M. R. et al. Chronology of Fabry-Perot interferometer fiber-optic sensors and their applications: a review. *Sensors* **14**, 7451–7488 (2014).

[11] 11. Lee, C. E. & Taylor, H. F. Interferometric optical fibre sensors using internal mirrors. *Electron. Lett.* **24**, 193–194 (1988).

[12] 12. Leiman, P. G. et al. Structure and morphogenesis of bacteriophage T4. *Cell. Mol. Life Sci.* **60**, 2356–2370 (2003).

[13] 13. Comeau, A. M. & Krisch, H. M. The capsid of the T4 phage superfamily: the evolution, diversity, and structure of some of the most prevalent proteins in the biosphere. *Mol. Biol. Evol.* **25**, 1321–1332 (2008).

[14] 14. Rossmann, M. G. et al. The bacteriophage T4 DNA injection machine. *Curr. Opin. Struct. Biol.* **14**, 171–180 (2004).

[15] 15. Kostyuchenko, V. A. et al. The tail structure of bacteriophage T4 and its mechanism of contraction. *Nat. Struct. Mol. Biol.* **12**, 810–813 (2005).

[16] 16. Taylor, N. M. I. et al. Structure of the T4 baseplate and its function in triggering sheath contraction. *Nature* **533**, 346–352 (2016).

[17] 17. Maruo, S. et al. Three-dimensional microfabrication with two-photon-absorbed photopolymerization. *Opt. Lett.* **22**, 132–134 (1997).

[18] 18. Kawata, S. et al. Finer features for functional microdevices. *Nature* **412**, 697–698 (2001).

[19] 19. Sugioka, K. & Cheng, Y. Ultrafast lasers—reliable tools for advanced materials processing. *Light Sci. Appl.* **3**, e149 (2014).

[20] 20. Zou, M. et al. Fiber-tip polymer clamped-beam probe for high-sensitivity nanoforce measurements. *Light Sci. Appl.* **10**, 171 (2021).

[21] 21. Wang, F. et al. Three-dimensional printed microcantilever with mechanical metamaterial for fiber-optic microforce sensing. *APL Photonics* **8**, 096108 (2023).

[22] 22. Wang, W. et al. High-precision surface-plasmon-resonance-based four-parameter optical fiber sensor for simultaneous detection of temperature, magnetic field, relative humidity, and voltage. *Chin. Opt. Lett.* **24**, 032601 (2026).

[23] 23. Wang, J. et al. Liquid crystal microcavity biosensors for real-time liver injury monitoring via whispering gallery mode laser. *Research* **8**, 0824 (2025).

[24] 24. Chen, Z. & Lu, C. Humidity sensors: a review of materials and mechanisms. *Sens. Lett.* **3**, 274–295 (2005).